RESEARCH ARTICLE
SPACE PHYSICS

Earth and Planetary Physics
9: 988–994, 2025
doi: 10.26464/epp2025050

Three-dimensional spectral analysis of gravity waves from airglow observations over Northwest China

QinZeng Li[1,2*], JiYao Xu[1,2], Wei Yuan[1], Xiao Liu[3], YaJun Zhu[1,2], and WeiJun Liu[1]

[1]State Key Laboratory of Solar Activity and Space Weather, National Space Science Center, Chinese Academy of Sciences, Beijing 100190, China;

[2]University of Chinese Academy of Sciences, Beijing 100049, China;

[3]School of Mathematics and Statistics, Henan Normal University, Xinxiang Henan 453000, China

Key Points:

- Seasonal variation characteristics of gravity waves (GWs) over Northwest China were first investigated by using the three-dimensional spectral analysis method.
- Gravity waves mainly propagate in the north and northeast directions in spring, summer, and autumn, and in the south direction in winter.
- The zonal propagation direction of GWs is controlled by the wind-filtering effect, whereas the meridional direction is mainly determined by the location of the wave source.

Citation: Li, Q. Z., Xu, J. Y., Yuan, W., Liu, X., Zhu, Y. J., and Liu, W. J. (2025). Three-dimensional spectral analysis of gravity waves from airglow observations over Northwest China. *Earth Planet. Phys.*, *9*(4), 988–994. http://doi.org/10.26464/epp2025050

Abstract: The three-dimensional spectral analysis method was applied to airglow data from September 2023 to August 2024 derived from an OH airglow imager located at the Hejing station (42.79°N, 83.73°E) to study the propagation characteristics of gravity waves (GWs) over Northwest China. We found that obvious seasonal variations occur in the propagation of GWs. In spring, GWs mainly propagate in the northeast direction. In summer and autumn, GWs mainly propagate in the north direction. However, GWs mainly propagate in the south direction in winter. The direction of GW propagation in the zonal direction is controlled by the wind-filtering effect, whereas the north–south meridional direction is mainly determined by the location of the wave source. We found that the average energy spectrum exhibits a 10%–20% higher intensity in summer and winter compared with spring and autumn. For the first time, we report the seasonal variation characteristics of GWs over the inland areas of Northwest China, which is of great significance for understanding the regional distribution characteristics of GWs.

Keywords: airglow; gravity wave; three-dimensional spectral analysis; seasonal variation

1. Introduction

Atmospheric gravity waves (GWs) are mainly generated by convection (Alexander and Holton, 2004; Li QZ et al., 2022; Nyassor et al., 2022; Franco-Diaz et al., 2024), wind shear (Pramitha et al., 2015), and cold fronts (Wrasse et al., 2024) in the lower atmosphere and orography (Liu X et al., 2019; Geldenhuys et al., 2021). Solar eclipses can also generate GWs (Gu SY et al., 2023). When GWs propagate upward to the mesopause, they break up and deposit momentum and energy in that region. Gravity waves play an important role in controlling the thermal and compositional structures and global circulation of the atmosphere (Lindzen, 1981; Fritts and Alexander, 2003; Gao HY et al., 2018; Ren DX et al., 2023).

Atmospheric GWs are widely studied by ground-based observation equipment, such as the radiosonde (Zhang SD et al., 2017), radar (Vargas et al., 2021), lidar (Ban C et al., 2015; Gong SH et al., 2015; Xue XH et al., 2020), and photometer (Ding F et al., 2004). These types of ground-based equipment can observe only the direction of the zenith. Although satellites can observe horizontally in two dimensions, the time resolution is limited. The all-sky airglow imaging device can compensate for the defects of imitations of these devices. When GWs pass through the airglow layer, they cause a disturbance (Ghodpage et al., 2016). The all-sky airglow imaging device detects this disturbance and provides two-dimensional, high-spatiotemporal resolution GW imaging observations. In the past, the main method for processing airglow was based on visual inspection (Wu Q and Killeen, 1996; Nakamura et al., 1999; Ejiri et al., 2003; Bageston et al., 2009; Li QZ et al., 2011, 2016, 2018), which resulted in recognition errors.

Matsuda et al. (2014) developed a spectral analysis method by converting the three-dimensional (3D) wavenumber space to the horizontal phase velocity space, resulting in a powerful spectral analysis tool for performing efficient statistical analysis of massive airglow images. This method can provide not only the propagation direction and horizontal phase velocity distribution of GWs, but

---

Correspondence to: Q. Z. Li, qzli@swl.ac.cn
Received 20 DEC 2024; Accepted 10 FEB 2025.

also the energy spectrum information. Recently, this method has been used for statistical research on GWs (Takeo et al., 2017; Tsuchiya et al., 2018; Kogure et al., 2023).

The terrain conditions in the inland areas of Northwest China are complex and unique, with deserts and high mountains. However, this area is considered the farthest from the coast, and the characteristics of GWs over this area have not been studied. In this study, we report for the first time the characteristics of GWs for this area by using the 3D spectral analysis method.

2. Observation and Method

2.1 Airglow Imager

Two sets of airglow imagers were operated at the Hejing station, Xinjiang, in August 2023. Figure 1 shows the location of the Hejing station (42.79°N, 83.73°E). These imagers are part of the Passive Optical Observation System for the Chinese Meridian Project Phase II Programme (Wang C et al., 2020). Every imager consists of a fish-eye lens (Focal length of 16 mm and aperture of f/4.0) with a field of view (FOV) of 180° and a cooled-CCD camera with a resolution of 1024 × 1024 pixels. The OH near-infrared band filter, which spans from 715 to 930 nm, features a notch centered at 865 ± 9 nm to block the O_2 (0, 1) emission line. In this study, we used images of the OH airglow emission with typical emission heights of ~87 km. The exposure time was set to 60 s for the OH image.

2.2 Analysis Method

Figure 2a shows a raw OH airglow image obtained at Hejing at 13:52:46 universal time (UT) on January 2, 2024. First, we applied a median filter with a window size of 15 × 15 pixels to the raw images to remove stars. Second, we removed the dark counts and offset values of the CCD, which were estimated in the areas near the four corners of the raw images outside the FOV. We assumed that the dark count was uniform over the CCD array. We then calculated the normalized perturbation of the airglow intensity ΔI,

$$\Delta I = \frac{I - \bar{I}}{\bar{I}}, \tag{1}$$

where I is the airglow intensity and $\bar{I}$ is the airglow intensity averaged over a ±30 min window. Third, we projected the processed images onto geographic coordinates with an area of 800 × 800 km, assuming a peak emission height of 87 km. Figure 2b shows the projected image from Figure 2a.

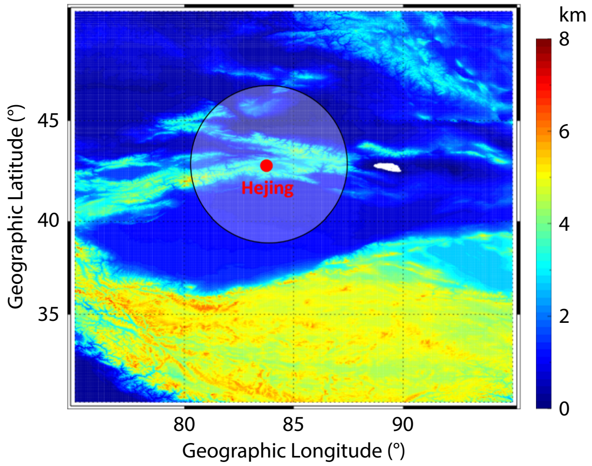

Figure 1. Location of the airglow imager station. The circle on the map gives the effective observation ranges of the OH airglow imager with a diameter of approximately 800 km. The background shows a map of the topography elevation from GTOPO30 (global digital elevation model with a horizontal grid spacing of 30 arc seconds).

Next, we calculated spectra of the zonal and meridional wavenumber and frequency by applying the 3D fast Fourier transform (FFT). Figure 2c shows the wavenumber spectrum of the OH images at Hejing from 13:34:07 to 14:04:01 UT on January 2, 2024. The wavenumber spectral domains (k, l, ω) were converted to horizontal phase velocity domains (v_x, v_y, ω) by using Equations (2) and (3) (Matsuda et al., 2014):

$$v_x = \frac{\omega k}{k^2 + l^2}, \tag{2}$$

$$v_y = \frac{\omega l}{k^2 + l^2}, \tag{3}$$

where k is the zonal wave number, and l is the meridional wave number, respectively, ω is the frequency, v_x and v_y are the zonal and meridional components of the horizontal phase velocity, respectively. The volume element conversion between the wavenumber spectral space and the horizontal phase velocity space is given by Equations (4) and (5):

$$\mathrm{d}v_x \mathrm{d}v_y \mathrm{d}\omega = \boldsymbol{J} \cdot \mathrm{d}k\mathrm{d}l\mathrm{d}\omega, \tag{4}$$

$$\boldsymbol{J} = \begin{vmatrix} \frac{\partial v_x}{\partial k} & \frac{\partial v_x}{\partial l} & \frac{\partial v_x}{\partial \omega} \\ \frac{\partial v_y}{\partial k} & \frac{\partial v_y}{\partial l} & \frac{\partial v_y}{\partial \omega} \\ 0 & 0 & 1 \end{vmatrix}. \tag{5}$$

Figure 2d shows the phase velocity spectrum converted from the wavenumber spectrum shown in Figure 2c. The phase velocity spectrum is distributed in the south and southwest directions (180°–225° clockwise from the north) with a peak of 60–100 m/s, which indicates that the main waves observed by the imager were south- and southwest-propagating waves with phase velocities of 20–90 m/s during the period of 13:34:07 to 14:04:01 UT on January 2, 2024.

3. Results and Discussion

3.1 Seasonal Variations of the Horizontal Phase Velocity Spectrum

In this study, the OH airglow data used for statistical analysis were obtained from the Hejing station during the period from September 2023 to August 2024. We defined spring as March to April (2 months), summer as May to August (4 months), autumn as September to October (2 months), and winter as November to February (4 months). Table 1 shows the seasonal distribution of clear observation times and the number of GW events. The clear-sky duration in Hejing is significantly longer in winter than in other seasons, as the other seasons are often characterized by cloudy and rainy weather. Therefore, the statistical analysis results of GWs in winter are more reliable than those in other seasons.

Figure 3 shows seasonal horizontal phase velocity spectra of

Table 1. The seasonal distribution of clear observation times and number of GW events.

	Spring	Summer	Autumn	Winter	Total
Total of clear observation times (h)	112	278	172	624	1186
Number of GW events	23	67	42	143	275

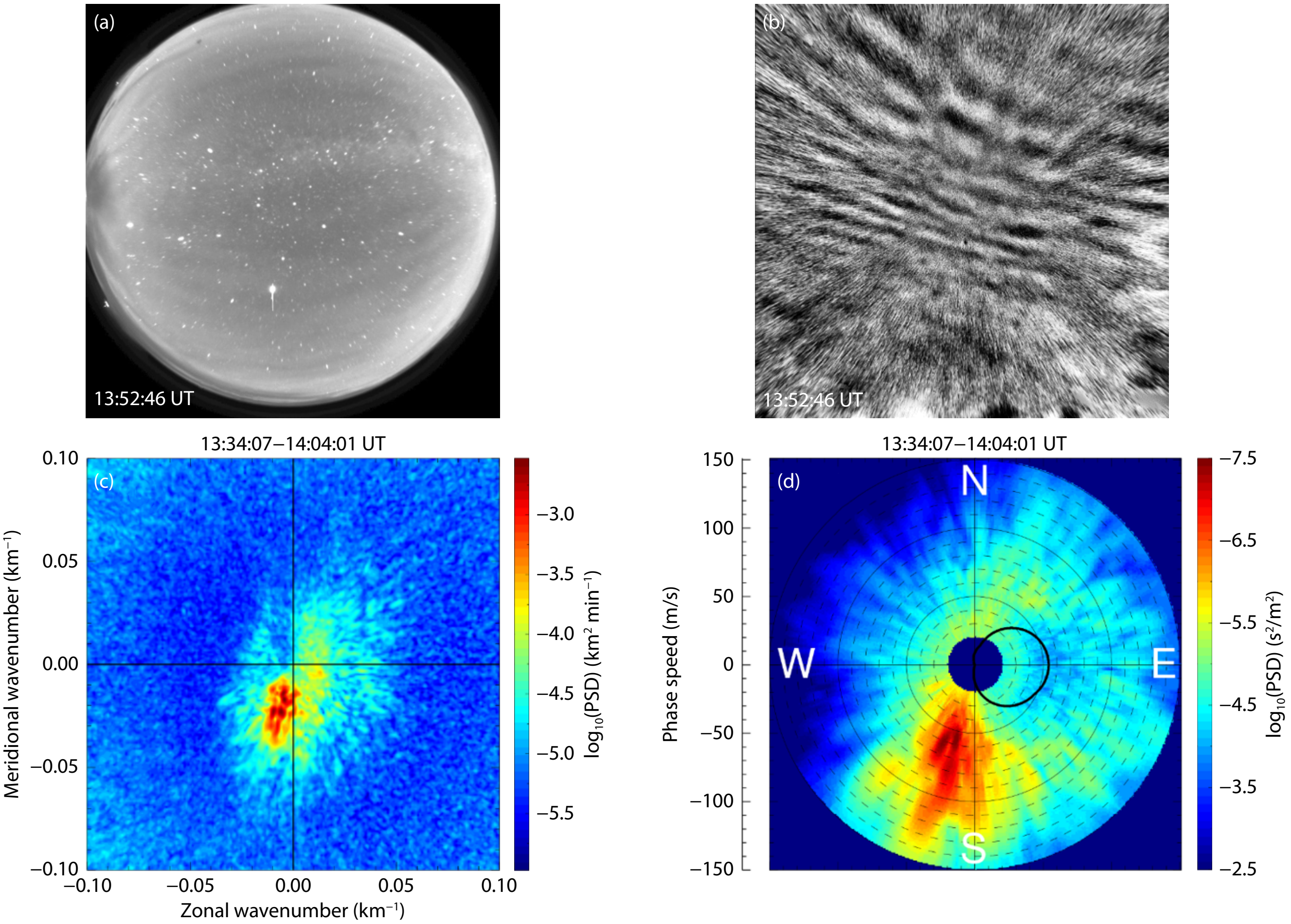

Figure 2. (a) A raw OH airglow image obtained at Hejing at 13:52:46 UT on January 2, 2024. (b) The processed image was projected to 800 × 800 km in geographic coordinates with northward to the top and eastward to the right. (c) The wavenumber spectrum of the OH images at Hejing at 13:34:07–14:04:01 UT on January 2, 2024. (d) The phase velocity spectrum (integrated over the frequency domain), converted from the wavenumber spectrum shown in (c).

mesospheric GWs seen in the OH images obtained at the Hejing station. The power spectral density (PSD) represents the power of GWs. The low-velocity region (0 to 20 m/s) is not shown because of white noise contamination of the airglow images. The PSD of horizontal phase velocity spectra for each season comes from the average of the selected time window. Obvious seasonal variation characteristics can be seen. The phase velocity spectrum is distributed in the north and northeast directions with phase velocities of 40–70 m/s in spring and northeastward with phase velocities of 30–100 m/s in summer. In autumn, the phase velocity spectrum is distributed in the northwest and northeast directions with phase velocities of 30–90 m/s. In winter, the phase velocity spectrum is distributed in the south and southeast directions with phase velocities of 40–110 m/s.

Figure 4 shows the average energy spectrum distribution with seasonal variation. We found that the average energy spectral intensity in summer and winter was higher than that in spring and autumn, with the highest in winter. This may be due to the active meteorological activity in the lower atmosphere during summer and winter.

3.2 Possible Mechanisms That Affect the Anisotropy of Wave Propagation

The convective system is the main source of GWs. We used the vertical fluid motion values provided by ERA5 (ECMWF Reanalysis v5; Hersbach et al., 2020), European Centre for Medium-Range Weather Forecasts (ECMWF), to study the strength of convective activity, where a negative pressure vertical velocity (upward motion) indicates relatively strong convective activity. Figure 5 shows seasonal averages of the tropospheric vertical flow velocity. Regions of strong upward velocities from the southwest direction

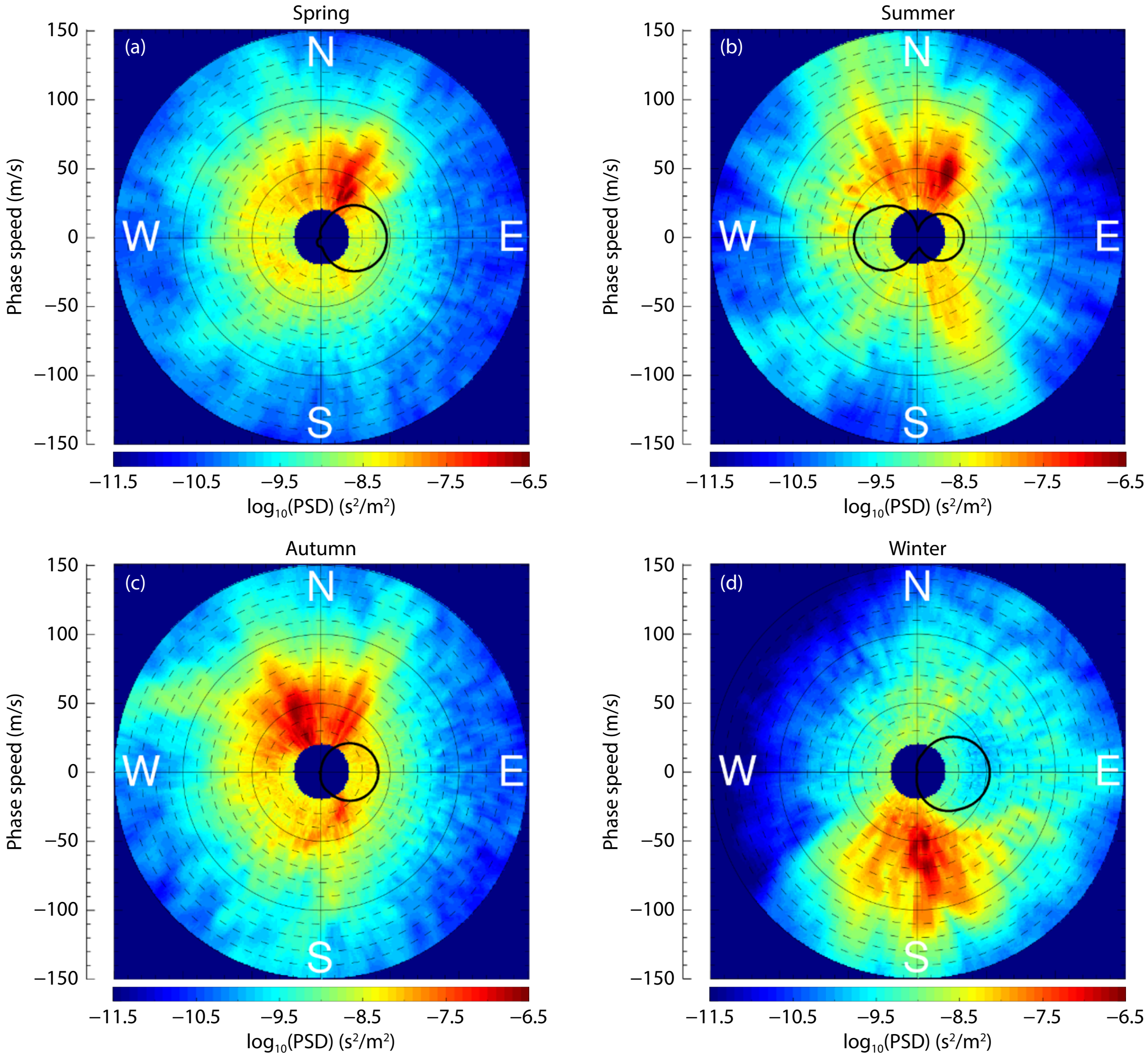

Figure 3. The seasonal horizontal phase velocity spectra of mesospheric GWs seen in OH images obtained at the Hejing station. The black circles represent blocking diagrams of the forbidden GW propagation region caused by wind filtering.

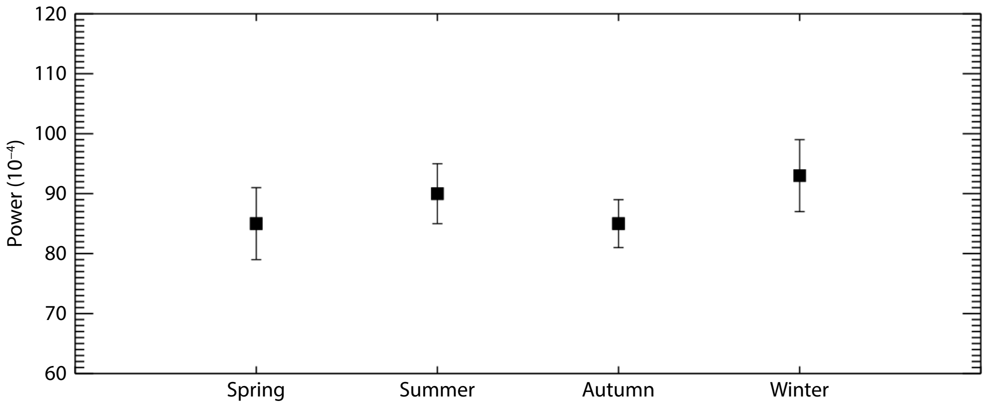

Figure 4. Average energy spectrum distribution with seasonal variation.

can be seen in spring, summer, and autumn. In autumn, strong convective activity appears over the Qinghai–Tibet Plateau southeast of the station. In winter, a region of strong vertical velocities appears north of the Hejing station. The GWs generated in this area will contribute to the southern propagation of GWs observed over the Hejing station. Therefore, the distribution of convective systems in different regions of the troposphere can explain the differences in the north–south propagation directions of GWs observed by the OH airglow imager.

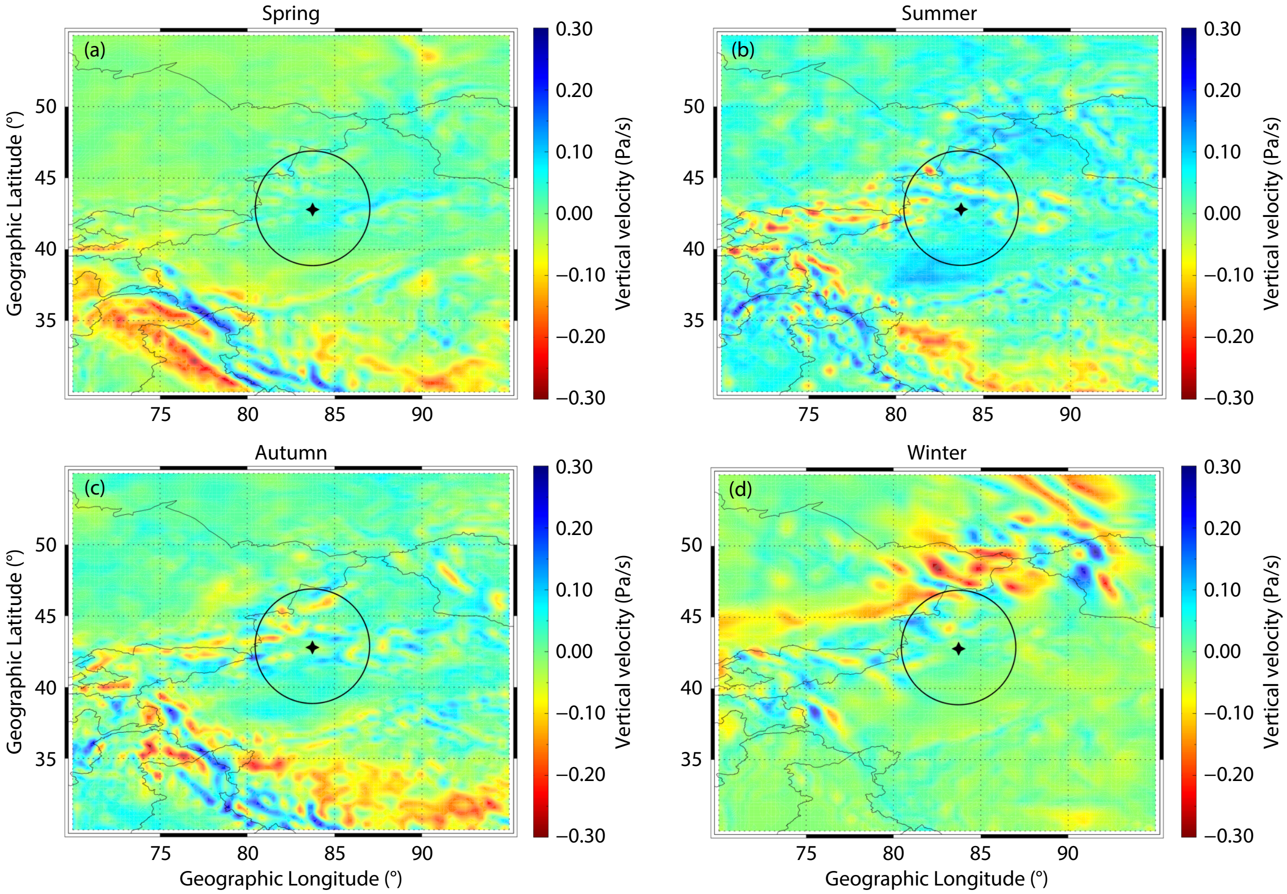

Figure 5. Seasonal averages of the tropospheric vertical flow velocity. These plots were obtained by averaging the upward flow data at 400 hPa (~7 km altitude) obtained by the ERA5, European Center for Medium-Range Forecasts, over the nights when we calculated the airglow spectra shown in Figure 3. The circle in each panel gives the effective observation ranges of the OH airglow imager with a diameter of approximately 800 km.

Regarding the difference in the direction of propagation between the east and the west, the filtering effect of the wind field may have played an important role. The dispersion relationship of GWs (Hines, 1960) is given by

$$m^2 = \frac{N^2}{(c-u)^2} - k_h - \frac{1}{4H^2}, \tag{6}$$

where m and k_h are vertical and horizontal wavenumbers, respectively; c is the horizontal observed phase speed of the GW; u is the background wind speed in the wave propagation direction; N is the Brunt–Väisälä frequency; and H is the scale height. According to Equation (6), if the GW propagation speed is close to or equal to the horizontal wind speed in the wave propagation, the vertical wave number m will become infinite, which means that when encountering a critical layer, GWs will not be able to propagate upward.

A blocking diagram is used to represent the velocity distribution, and the GWs in this distribution area cannot propagate to a specific height because of the critical layer filtering effect. The blocking diagram is generated by the following equation:

$$c = V_z \cos\varphi + V_m \sin\varphi, \tag{7}$$

where V_z and V_m are the zonal and meridional wind speed, respectively, and φ is the azimuth (anticlockwise from the east) of the horizontal propagation direction.

Because of the lack of simultaneous wind field observations, the wind field in the altitude range of 0 to 80 km comes from ERA5, and the wind field in the range of 80 to 87 km comes from horizontal wind model-14 (HWM14; Drob et al., 2015). Figure 6a shows a 3D blocking diagram (Taylor et al., 1993) from 0 to 87 km on January 2, 2024. Figure 6b shows the 2D blocking diagram from Figure 6a. Two-dimensional blocking diagrams are superimposed on the horizontal velocity spectrum in Figure 3. From Figure 3, it can be seen that almost no GW spectrum is present in the blocking diagram area, which is quite consistent with the critical layer filtering theory.

Gravity waves generated in the lower atmosphere in this forbidden region will be filtered out and cannot be observed by the airglow imager. However, GWs generated through secondary waves in the stratosphere may not be filtered out by wind fields. Another scenario exists in which GWs can propagate thousands of kilometers through ducts (Xu JY et al., 2015; Li QZ et al., 2024). Therefore, some GWs within the forbidden region probably did not originate from altitudes below the OH airglow layer, but from a location far away from the station by using ducts distributed at the height of the mesopause region.

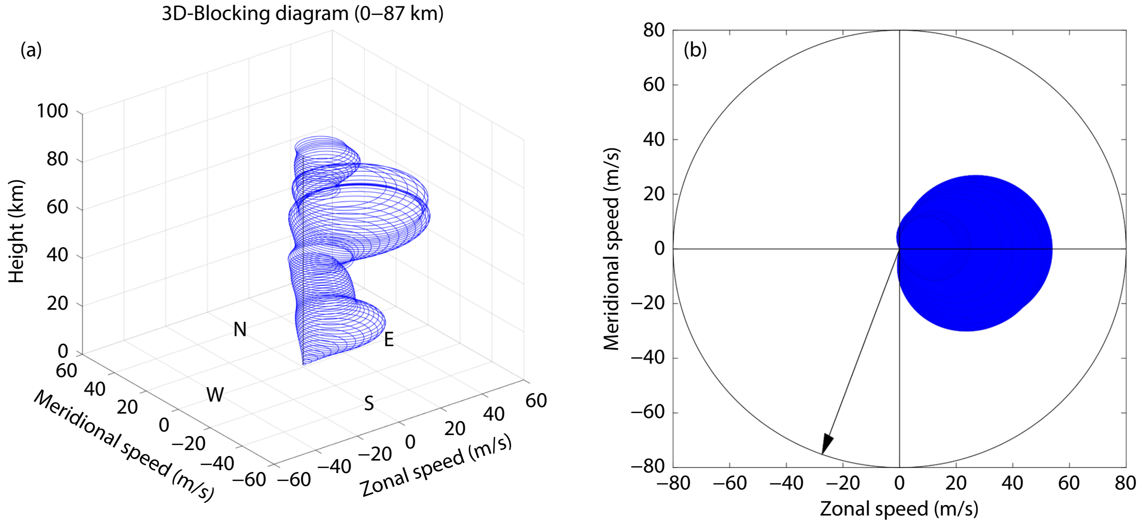

Figure 6. (a) Three-dimensional blocking diagram from 0 to 87 km on January 2, 2024. The wind field used from 0 to 80 km comes from ERA5, and that from 80 to 87 km comes from the HWM14 model. (b) The 2D blocking diagram from (a). The arrow in (b) represents the magnitude and direction of the GW.

From the aforementioned analysis, we found that the convective systems and wind-field filtering control the seasonal variation characteristics of GW propagation above the Hejing station. Another factor that cannot be ignored is the topographic condition. The Hejing station is located in the Tianshan Mountains. Here, the terrain can generate stationary mountain waves. However, the mountain waves generated by the Tianshan Mountains can be broken in the stratospheric region to produce secondary waves, which are also an important source of GWs (Liu X et al., 2019). In future work, we will focus on the impact of mountain waves in the Tianshan region on the middle and upper atmosphere.

4. Conclusions

We analyzed the propagation characteristics of GWs by using the 3D spectral analysis method for OH all-sky airglow imager data obtained from the Hejing station. We provide, for the first time, the seasonal variation characteristics of GWs over the region of Northwest China.

We found obvious seasonal variations in the propagation of GWs. Gravity waves mainly propagate in the southern direction in winter; however, they mainly propagate in the northern direction in spring, summer, and autumn. The zonal propagation direction of GWs is controlled by the wind-filtering effect, whereas the meridional direction is mainly determined by the location of the wave source. We also found that the mean energy spectral intensity during summer and winter is approximately 10%–20% greater than that in spring and autumn. This study is of great significance for understanding the distribution characteristics of GWs over the inland areas of Northwest China.

Acknowledgments

This work was supported by the National Science Foundation of China (Grant Nos. 42374205 and 41974179) and the Specialized Research Fund of the National Space Science Center, Chinese Academy of Sciences (Grant No. E4PD3010). The project was also supported by the Specialized Research Fund for State Key Laboratories. We acknowledge the use of data from the Chinese Meridian Project.

References

Alexander, M. J., and Holton, J. R. (2004). On the spectrum of vertically propagating gravity waves generated by a transient heat source. *Atmos. Chem. Phys.*, *4*(4), 923–932. https://doi.org/10.5194/acp-4-923-2004

Bageston, J. V., Wrasse, C. M., Gobbi, D., Takahashi, H., and Souza, P. B. (2009). Observation of mesospheric gravity waves at Comandante Ferraz Antarctica Station (62°S). *Ann. Geophys.*, *27*(6), 2593–2598. https://doi.org/10.5194/angeo-27-2593-2009

Ban, C., Li, T., Fang, X., Dou, X. K., and Xiong, J. G. (2015). Sodium lidar-observed gravity wave breaking followed by an upward propagation of sporadic sodium layer over Hefei, China. *J. Geophys. Res.: Space Phys.*, *120*, 7958–7969. https://doi.org/10.1002/2015JA021339

Ding F., Yuan, H., Wan, W. X., Reid, I. M., and Woithe, J. M. (2004). Occurrence characteristics of medium-scale gravity waves observed in OH and OI nightglow over Adelaide (34.5°S, 138.5°E). *J. Geophys. Res.: Atmos.*, *109*(D14), D14104. https://doi.org/10.1029/2003JD004096

Drob, D. P., Emmert, J. T., Meriwether, J. W., Makela, J. J., Doornbos, E., Conde, M., Hernandez, G., Noto, J., Zawdie, K. A., … Klenzing, J. H. (2015). An update to the Horizontal Wind Model (HWM): The quiet time thermosphere. *Earth Space Sci.*, *2*(7), 301–319. https://doi.org/10.1002/2014EA000089

Ejiri, M. K., Shiokawa, K., Ogawa, T., Igarashi, K., Nakamura, T., and Tsuda, T. (2003). Statistical study of short-period gravity waves in OH and OI nightglow images at two separated sites. *J. Geophys. Res.: Atmos.*, *108*(D21), 4679. https://doi.org/10.1029/2002JD002795

Franco-Diaz, E., Gerding, M., Holt, L., Strelnikova, I., Wing, R., Baumgarten, G., and Lübken, F. J. (2024). Convective gravity wave events during summer near 54°N, present in both AIRS and Rayleigh-Mie-Raman (RMR) lidar observations. *Atmos. Chem. Phys.*, *24*(2), 1543–1558. https://doi.org/10.5194/acp-24-1543-2024

Fritts, D. C., and Alexander, M. J. (2003). Gravity wave dynamics and effects in the middle atmosphere. *Rev. Geophys.*, *41*(1), 1003. https://doi.org/10.1029/2001RG000106

Gao, H. Y., Li, L. C., Bu, L. B., Zhang, Q. L., Tang, Y. H., and Wang, Z. (2018). Effect of small-scale gravity waves on polar mesospheric clouds observed from CIPS/AIM. *J. Geophys. Res.: Space Phys.*, *123*(5), 4026–4045. https://doi.org/10.1029/2017JA024855

Geldenhuys, M., Preusse, P., Krisch, I., Zülicke, C., Ungermann, J., Ern, M., Friedl-Vallon, F., and Riese, M. (2021). Orographically induced spontaneous imbalance within the jet causing a large-scale gravity wave event. *Atmos. Chem. Phys.*, *21*(13), 10393–10412. https://doi.org/10.5194/acp-21-10393-2021

Ghodpage, R. N., Hickey, M. P., Taori, A. K., Siingh, D., and Patil, P. T. (2016). Response of OH airglow emissions to mesospheric gravity waves and comparisons with full-wave model simulation at a low-latitude Indian station. *Atmos. Chem. Phys.*, *16*(9), 5611–5621. https://doi.org/10.5194/acp-16-5611-2016

Gong, S. H., Yang, G. T., Dou, X. K., Xu, J. Y., Chen, C. X., and Gong, S. S. (2015). Statistical study of atmospheric gravity waves in the mesopause region observed by a Lidar Chain in Eastern China. *J. Geophys. Res.: Atmos.*, *120*(15), 7619–7634. https://doi.org/10.1002/2014JD022673

Gu, S. Y., Yang, Z. L., Qin, Y. S., Teng, C. K. M., Dou, X. K., Lei, J. H., Huang, F. Q., Dang, T., and Sun, W. J. (2023). Ionospheric TEC variation and gravity waves signatures during the solar eclipse on 21 June 2020 over southern China. *J. Geophys. Res.: Space Phys.*, *128*(1), e2022JA030758. https://doi.org/10.1029/2022JA030758

Hersbach, H., Bell, B., Berrisford, P., Hirahara, S., Horányi, A., Muñoz-Sabater, J., Nicolas, J., Peubey, C., Radu, R., … Thépaut, J. N. (2020). The ERA5 global reanalysis. *Quart. J. Roy. Meteorol. Soc.*, *146*(730), 1999–2049. https://doi.org/10.1002/qj.3803

Hines, C. O. (1960). Internal atmospheric gravity waves at ionospheric heights. *Can. J. Phys.*, *38*(11), 1441–1481. https://doi.org/10.1139/p60-150

Kogure, M., Nakamura, T., Murphy, D. J., Taylor, M. J., Zhao, Y. C., Pautet, P. D., Tsutsumi, M., Tomikawa, Y., Ejiri, M. K., and Nishiyama, T. (2023). Characteristics of gravity wave horizontal phase velocity spectra in the mesosphere over the Antarctic stations, Syowa and Davis. *J. Geophys. Res.: Atmos.*, *128*(6), e2022JD037751. https://doi.org/10.1029/2022JD037751

Li, Q. Z., Xu, J. Y., Yue, J., Yuan, W., and Liu, X. (2011). Statistical characteristics of gravity wave activities observed by an OH airglow imager at Xinglong, in northern China. *Ann. Geophys.*, *29*(8), 1401–1410. https://doi.org/10.5194/angeo-29-1401-2011

Li, Q. Z., Xu, J. Y., Liu, X., Yuan, W., and Chen, J. S. (2016). Characteristics of mesospheric gravity waves over the southeastern Tibetan Plateau region. *J. Geophys. Res.: Space Phys.*, *121*(9), 9204–9221. https://doi.org/10.1002/2016JA022823

Li, Q. Z., Yusupov, K., Akchurin, A., Yuan, W., Liu, X., and Xu, J. Y. (2018). First OH airglow observation of mesospheric gravity waves over European Russia region. *J. Geophys. Res.: Space Phys.*, *123*(3), 2168–2180. https://doi.org/10.1002/2017JA025081

Li, Q. Z., Xu, J. Y., Liu, H. L., Liu, X., and Yuan, W. (2022). How do gravity waves triggered by a typhoon propagate from the troposphere to the upper atmosphere?. *Atmos. Chem. Phys.*, *22*(18), 12077–12091. https://doi.org/10.5194/acp-22-12077-2022

Li, Q. Z., Xu, J. Y., Gusman, A. R., Liu, H. L., Yuan, W. J., Liu, W., Zhu, Y. J., and Liu, X. (2024). Upper-atmosphere responses to the 2022 Hunga Tonga–Hunga Ha'apai volcanic eruption via acoustic gravity waves and air–sea interaction. *Atmos. Chem. Phys.*, *24*(14), 8343–8361. https://doi.org/10.5194/acp-24-8343-2024

Lindzen, R. S. (1981). Turbulence and stress owing to gravity wave and tidal breakdown. *J. Geophys. Res.: Oceans*, *86*(C10), 9707–9714. https://doi.org/10.1029/jc086ic10p09707

Liu, X., Xu, J. Y., Yue, J., Vadas, S. L., and Becker, E. (2019). Orographic primary and secondary gravity waves in the middle atmosphere from 16-year SABER observations. *Geophys. Res. Lett.*, *46*(8), 4512–4522. https://doi.org/10.1029/2019GL082256

Matsuda, T. S., Nakamura, T., Ejiri, M. K., Tsutsumi, M., and Shiokawa, K. (2014). New statistical analysis of the horizontal phase velocity distribution of gravity waves observed by airglow imaging. *J. Geophys. Res.: Atmos.*, *119*(16), 9707–9718. https://doi.org/10.1002/2014JD021543

Nakamura, T., Higashikawa, A., Tsuda, T., and Matsushita, Y. (1999). Seasonal variations of gravity wave structures in OH airglow with a CCD imager at Shigaraki. *Earth Planets Space*, *51*(7-8), 897–906. https://doi.org/10.1186/BF03353248

Nyassor, P. K., Wrasse, C. M., Paulino, I., São Sabbas, E. F. M. T., Bageston, J. V., Naccarato, K. P., Gobbi, D., Figueiredo, C. A. O. B., Ayorinde, T. T., … Barros, D. (2022). Sources of concentric gravity waves generated by a moving mesoscale convective system in southern Brazil. *Atmos. Chem. Phys.*, *22*(23), 15153–15177. https://doi.org/10.5194/acp-22-15153-2022

Pramitha, M., Venkat Ratnam, M., Taori, A., Krishna Murthy, B. V., Pallamraju, D., and Rao, S. V. B. (2015). Evidence for tropospheric wind shear excitation of high-phase-speed gravity waves reaching the mesosphere using the ray-tracing technique. *Atmos. Chem. Phys.*, *15*(5), 2709–2721. https://doi.org/10.5194/acp-15-2709-2015

Ren, D. X., Lei, J. H., Liu, H. L., Wang, W. B., Yue, J., and Liu, H. X. (2023). Influence of mesospheric gravity wave drag on the formation of winter helium bulge in the thermosphere. *J. Geophys. Res.: Space Phys.*, *128*(2), e2022JA031022. https://doi.org/10.1029/2022JA031022

Takeo, D., Shiokawa, K., Fujinami, H., Otsuka, Y., Matsuda, T. S., Ejiri, M. K., Nakamura, T., and Yamamoto, M. (2017). Sixteen year variation of horizontal phase velocity and propagation direction of mesospheric and thermospheric waves in airglow images at Shigaraki, Japan. *J. Geophys. Res.: Space Physics*, *122*(8), 8770–8780. https://doi.org/10.1002/2017JA023919

Taylor, M. J., Ryan, E. H., Tuan, T. F., and Edwards, R. (1993). Evidence of preferential directions for gravity wave propagation due to wind filtering in the middle atmosphere. *J. Geophys. Res.: Atmos.*, *98*(A4), 6047–6057. https://doi.org/10.1029/92JA02604

Tsuchiya, S., Shiokawa, K., Fujinami, H., Otsuka, Y., Nakamura, T., and Yamamoto, M. (2018). Statistical analysis of the phase velocity distribution of mesospheric and ionospheric waves observed in airglow images over a 16-year period: Comparison between Rikubetsu and Shigaraki, Japan. *J. Geophys. Res.: Space Phys.*, *123*(8), 6930–6947. https://doi.org/10.1029/2018JA025585

Vargas, F., Chau, J. L., Asokan, H. C., and Gerding, M. (2021). Mesospheric gravity wave activity estimated via airglow imagery, multistatic meteor radar, and SABER data taken during the SIMONe–2018 campaign. *Atmos. Chem. Phys.*, *21*(17), 13631–13654. https://doi.org/10.5194/acp-21-13631-2021

Wang, C., Chen, Z. Q., and Xu, J. Y. (2020). Introduction to Chinese Meridian Project–Phase II. *Chin. J. Space Sci.*, *40*(5), 718–722. https://doi.org/10.11728/cjss2020.05.718

Wrasse, C. M., Nyassor, P. K., Da Silva, L. A., Figueiredo, C. A. O. B., Bageston, J. V., Naccarato, K. P., Barros, D., Takahashi, H., and Gobbi, D. (2024). Studies on the propagation dynamics and source mechanism of quasi-monochromatic gravity waves observed over São Martinho da Serra (29°S, 53°W), Brazil. *Atmos. Chem. Phys.*, *24*(9), 5405–5431. https://doi.org/10.5194/acp-24-5405-2024

Wu, Q., and Killeen, T. L. (1996). Seasonal dependence of mesospheric gravity waves (<100 Km) at Peach Mountain Observatory, Michigan. *Geophys. Res. Lett.*, *23*(17), 2211–2214. https://doi.org/10.1029/96GL02168

Xu, J. Y., Li, Q. Z., Yue, J., Hoffmann, L., Straka III, W. C., Wang, C. M., Liu, M. H., Yuan, W., Han, S., … Ning, B. Q. (2015). Concentric gravity waves over northern China observed by an airglow imager network and satellites. *J. Geophys. Res.: Atmos.*, *120*(21), 11058–11078. https://doi.org/10.1002/2015JD023786

Xue, X. H., Sun, D. S., Xia, H. Y., and Dou, X. K. (2020). Inertial gravity waves observed by a Doppler wind LiDAR and their possible sources. *Earth Planet. Phys.*, *4*(5), 461–471. https://doi.org/10.26464/epp2020039

Zhang, S. D., Huang, C. M., Huang, K. M., Gong, Y., Chen, G., Gan, Q., and Zhang, Y. H. (2017). Latitudinal and seasonal variations of vertical wave number spectra of three-dimensional winds revealed by radiosonde observations. *J. Geophys. Res.: Atmos.*, *122*(24), 13174–13190. https://doi.org/10.1002/2017JD027602